RESEARCH ARTICLE

Energy & Environmental Materials WILEY

Lithium-Metal Free Sulfur Battery

Lithium-Metal Free Sulfur Battery Based on Waste Biomass Anode and Nano-Sized Li_2S Cathode

*Pejman Salimi, Eleonora Venezia, Somayeh Taghavi, Sebastiano Tieuli, Lorenzo Carbone, Mirko Prato, Michela Signoretto, Jianfeng Qiu, and Remo Proietti Zaccaria**

The realization of a stable lithium-metal free (LiMF) sulfur battery based on amorphous carbon anode and lithium sulfide (Li_2S) cathode is here reported. In particular, a biomass waste originating full-cell combining a carbonized brewer's spent grain (CBSG) biochar anode with a Li_2S-graphene composite cathode (Li_2S70Gr30) is proposed. This design is particularly attractive for applying a cost-effective, high performance, environment friendly, and safe anode material, as an alternative to standard graphite and metallic lithium in emerging battery technologies. The anodic and cathodic materials are characterized in terms of structure, morphology and composition through X-ray diffraction, scanning and transmission electron microscopy, X-ray photoelectron and Raman spectroscopies. Furthermore, an electrochemical characterization comprising galvanostatic cycling, rate capability and cyclic voltammetry tests were carried out both in half-cell and full-cell configurations. The systematic investigation reveals that unlike graphite, the biochar electrode displays good compatibility with the electrolyte typically employed in sulfur batteries. The CBSG/Li_2S70Gr30 full-cell demonstrates an initial charge and discharge capacities of 726 and 537 mAh g^{-1}, respectively, at 0.05C with a coulombic efficiency of 74%. Moreover, it discloses a reversible capacity of 330 mAh g^{-1} (0.1C) after over 300 cycles. Based on these achievements, the CBSG/Li_2S70Gr30 battery system can be considered as a promising energy storage solution for electric vehicles (EVs), especially when taking into account its easy scalability to an industrial level.

1. Introduction

To date, high power/energy densities have been considered as the most important parameters for a valuable energy storage device for applications such as electric vehicles (EVs), portable electronic devices and stationary storage systems. Recently, a new need has however entered in the energy storage field, that is the requirement of environment friendly electrochemical energy storage devices (EESDs).[1] In this regard, their implementation in the global automotive market could truly contribute to reduce the employment of fossil-fuel-based vehicles tackling the negative impact of CO_2 emissions according to the European Protocol in the Transportation Sector[2,3] and, at the same time, to reduce the production of dangerous chemicals often coming with exhausted standard secondary batteries. Nowadays, lithium-ion batteries (LIBs) are the main power source of EVs.[4,5] However, the limited transport range of EVs powered by current LIBs (up to about 400–450 km under ideal conditions), with an energy density of around 250 Wh kg^{-1}, is the main barrier preventing the spreading of electric transportation.[6] In this scenario, lithium-sulfur batteries (LSBs), a subgroup of LIBs, are considered as one of the most promising alternatives to current lithium-ion based technologies. Their high theoretical gravimetrical energy density of 2600 Wh kg^{-1} [7] and low-cost are expected to boost the EVs penetration in the global auto market. Importantly, sulfur is also naturally abundant and environment friendly, and when coupled with lithium, it realizes a remarkable theoretical specific capacity, as high as 1675 mAh g^{-1}. The chemical reaction describing the lithium-sulfur interaction is:[8,9]

$$S_8 + 16Li^+ + 16e^- \leftrightarrow 8Li_2S \quad (1)$$

Even though very promising, a series of obstacles have however hindered the commercialization of lithium-sulfur systems.[10] One main concern is related to the safety issue associated with the use of metallic lithium.[11] Moreover, the formation and growth of lithium dendrites during the charge process on the lithium surface leads to a short circuit causing premature cell failure.[12] On the cathode side, the large volume expansion and low ionic and electronic conductivity of sulfur together with the formation of lithium sulfide (Li_2S) as discharge product, cause polarization increase during the charge/discharge processes.[13,14] Another major hurdle to the practical use of LSBs arises from the high

P. Salimi, E. Venezia, Dr. L. Carbone, Dr. M. Prato, Prof. R. Proietti Zaccaria
Istituto Italiano di Tecnologia, via Morego 30, Genoa 16163, Italy
E-mail: remo.proietti@iit.it
P. Salimi, E. Venezia
Department of Chemistry and Industrial Chemistry, University of Genova, via Dodecaneso 31 I-16146, Genoa Italy
Dr. S. Taghavi, Dr. S. Tieuli, Prof. M. Signoretto
CATMAT Lab, Department of Molecular Sciences and Nanosystems, Ca' Foscari University Venice and INSTM Consortium, RU of Venice, Via Torino 155 30172, Venezia Mestre Italy
Prof. J. Qiu, Prof. R. Proietti Zaccaria
Department of Physics, Shaoxing University, Shaoxing 312000, China
The ORCID identification number(s) for the author(s) of this article can be found under https://doi.org/10.1002/eem2.12567.

DOI: 10.1002/eem2.12567

solubility of lithium polysulfides (PSs) in organic solvents.[8] The dissolution of these species within the electrolyte leads to irreversible loss of sulfur active material due to the so-called 'shuttle effect' thus leading to a rapid capacity fade and short cycle life.[15] In order to overcome the aforementioned shortcomings, the lithiated counterpart of sulfur, i.e. Li_2S, could be used as alternative cathode material.[16] Indeed, Li_2S-based cathodes can be paired with various anode materials beyond lithium metal thus leading to a safe lithium-metal free (LiMF) battery.[17–19] Specifically, Li_2S can deliver a theoretical specific capacity of 1166 mAh g^{-1}[20] which, even though lower than the 1675 mAh g^{-1} of LSBs, remains a very attractive value when compared with current technology. Furthermore, Li_2S possesses higher thermal stability compared with sulfur showing a melting point of 938 °C,[21] and does not exhibit any volumetric expansion in the initial charge process.[12,22] Nonetheless, the low electronic and ionic conductivity of Li_2S, together with the formation of PSs in the cathode, still remain crucial challenges to be addressed, as they lead to high charge transfer resistance at the interface between the Li_2S cathode and electrolyte as well as to poor cycling stability of the cell.[16] Moreover, another challenge related to the use of Li_2S as cathode active material is the high initial activation barrier that has to be overcome during the first charge process.[23] Indeed, the conversion of Li_2S to sulfur as S_8 involves a large overpotential due to the polysulfides phase nucleation, thus requiring the cell activation at 3.5 V.[24] Many approaches have been evaluated in order to lower this kinetic barrier, such as downsizing the Li_2S particles,[25] combination with carbonaceous materials,[20] optimizing the electrolyte composition,[26] and reducing the current rate.[27] In this work, a simple recrystallization method has been employed to realize a Li_2S-few layer graphene composite material thus combining the positive effects associated to the use of a carbonaceous matrix (which increases the electrode conductivity and consequently the active material utilization) and small-sized Li_2S particles (thus reducing the activation barrier). It is worth pointing out that the as-prepared electrode does not require any activation cycle at high potential.

Similarly to the cathode, also the anode plays an important role in addressing the fundamental limitations of LSBs including safety issues and low energy density during long-term cycling. In order to face these issues, anode materials such as graphite, silicon, tin, and metal/metal oxide nanoparticles can be used aside metallic lithium.[28–32] However, these materials are usually expensive and not environment friendly.[33] For instance, metal oxide nanoparticles release toxic ions, with consequent damage of the living organisms.[34,35] On the other hand, graphite as one of the most employed anode materials in LIBs, undergoes exfoliation in conventional ether-based electrolytes, thus making it unsuitable for metallic lithium replacement[36,37] (ether-based electrolytes are needed for sulfur-based batteries as sulfur is not stable in traditional carbonate-based electrolytes[38,39]). Therefore, it is urgent to find an anode material combining safety, environment friendliness, low cost and high performance that can be compatible with ether-based electrolytes.

In this regard, biochars derived from pyrolysis of waste biomasses are promising alternatives to the standard graphite electrode for EESDs. The main advantage of these materials is their non-graphitizable structure with amorphous/pseudo-graphitic nanodomains,[40] which is favorable condition for electrochemical reactions in LIBs. Furthermore, the precursors of biochar are mainly renewable, green, cheap and abundant materials.[41] Following our previous studies,[42,43] we unveiled the enormous potential associated with the green re-use of wasting materials in EESDs. In this scenario, we suggest the use of carbon material derived from brewer's spent grain (BSG), an abundant solid industrial waste, to address the technical challenges related to anode electrodes in LSBs. In particular, the carbon material is obtained through a simple pyrolysis process from BSG. As reported by Luna-Lama et al.,[44] the evaluation of potential scalability requires a deep analysis where the cost of residue biomass, the availability of the feedstock, the simplicity of the procedure as well as the employed solvents and reagents, should be carefully taken into account. In view of these considerations, the methodology proposed in the present work could be considered potentially scalable to an industrial level due to the low cost and readily available feedstock.

Through the thermochemical decomposition in an inert atmosphere (pyrolysis process), BSG is converted into bio-oil and bio-gas and produces carbon-rich solid residues, named biochar. In the current study, we found that BSG-based electrodes could contribute to the design of stable long-term LSBs with the possibility of replacing nowadays anodes. The achieved stable electrochemical behavior of the proposed BSG-derived carbon material could be attributed to different factors: i) wider average interlayer spacing with respect to graphite, ii) presence of pyridinic N and quaternary N atoms along with oxygen groups, and iii) cross-linked carbonaceous clusters. Indeed, the increased interlayer spacing can lead to a greater Li-ions storage within the carbon structure, the functional groups can increase the conductivity of the carbon material while introducing extra free electrons next to the carbon atoms that accelerate the redox reactions,[45–47] and the cross-linked structures provide the biochar with extraordinary stability in ether-based electrolytes.[48]

Herein, we investigate Carbonized BSG (CBSG) anode and Li_2S-graphene composite cathode ($Li_2S70Gr30$) for designing a functional LiMF battery. The fabricated full-cell reveals a stable cycling behavior, showing a specific capacity of ~250 mAh g^{-1} over 300 cycles at 1C and a reversible capacity of 330 mAh g^{-1} at 0.1C after the rate capability test.

2. Results and Discussion

2.1. Materials Characterization

The elemental analysis of the CBSG anode was performed to determine the weight percentage of C, N, H, S, and O in the sample, with the values reported in **Table 1**. The C, N, H, and O amounts resulted to be 73.6, 4.7, 1.9 and 12.9 wt%, respectively. The S content is instead negligible with values below 1 wt%. The presence of N and O within the sample is known to contribute to the expansion of the interlayer spacing of the graphitic carbon domains, thus providing extra active sites for accommodating Li-ions.[49] Furthermore, the hybridization of N lone pair electrons with the π electrons of C increases the

Table 1. Elemental analysis of CBSG.

Sample [%]	C	N	H	S	O	Ash
CBSG	73.6	4.7	1.9	0.1	12.9	6.8

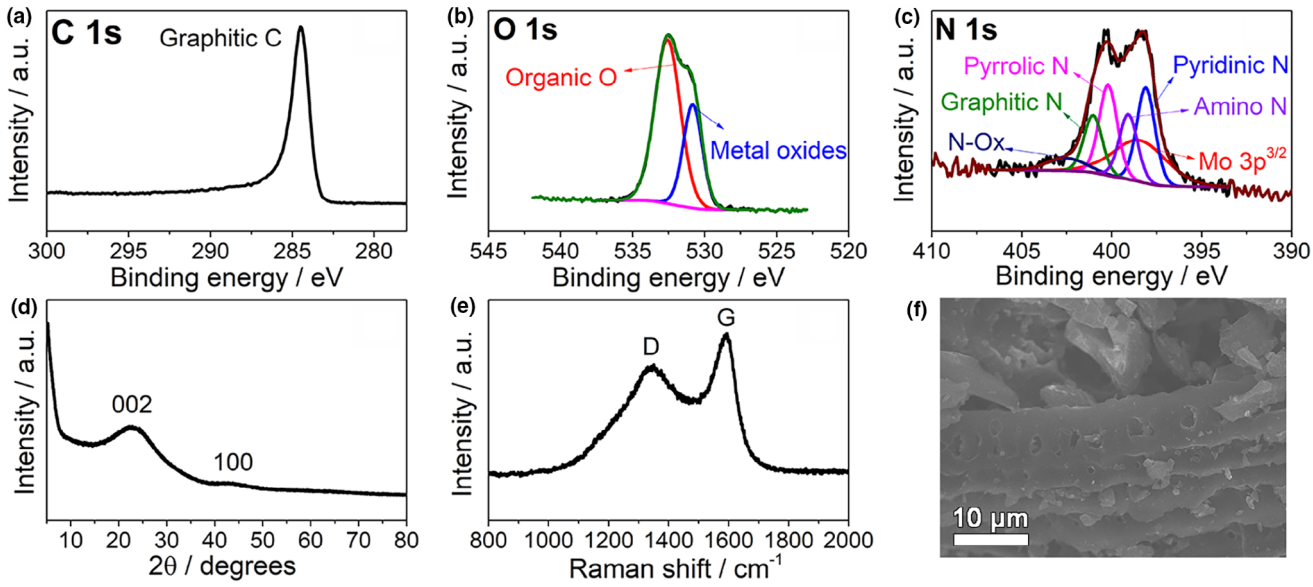

Figure 1. X-ray photoelectron spectroscopy (XPS) spectra of CBSG material relative to: a) C 1s, b) O 1s, and c) N 1s spectra. d) XRD pattern, e) Raman spectrum and f) FESEM of CBSG sample.

electronegativity of the electrode forming favorable binding sites for Li storage.[41] Finally, it has been recognized that Li-ions can bind in the vicinity of H atoms in CBSG electrodes.[50]

The functional and doped groups of CBSG were qualitatively analyzed by FTIR (see Figure S1, Supplementary Information) and X-ray photoelectron spectroscopy (XPS) (**Figure 1**). The FTIR analysis discloses the presence of aromatic C=C and C=O, and also the stretching of C=O groups of conjugated ketones and quinones. Additionally, the existence of N–C group, N–COO group, and C–O bonds of phenol, alcohol, ether bridging, aromatic rings, are identified with the FTIR technique. Figure 1a–c presents X-ray photoemission high-resolution spectra on oxygen, and nitrogen together with the results of the best-fit procedure. The analysis of the O 1s region suggests that O is bound to carbon in organic and metal-oxides forms. The XPS spectrum of N 1s also reveals the presence of N atoms in different coordination modes such as pyridinic N, amino N, pyrrolic N, and graphitic N. Finally, it is worth noting that XPS shows the presence of traces of other elements besides C, N, H and O, such as Mo, Cl, Si, In, Al, Pb and Ca (they are grouped as Ash in Table 1).

X-ray diffractometer and Raman analyses were carried out to determine the order/disorder degree and defects of the carbon layers of CBSG. The XRD pattern of Figure 1d shows a pronounced peak at around $2\theta = 23°$ and a weak one at around $2\theta = 44°$, corresponding to the (002) and (100) planes, respectively.[47] The relatively low intensity and broad shape of the peaks reflect the amorphous feature of the CBSG.[49] The Raman spectrum of Figure 1e displays the presence of two prominent peaks at around 1350 cm^{-1} (D-band) and 1600 cm^{-1} (G-band) corresponding to disordered or turbostratic structure and sp^2-hybridized carbon of CBSG, respectively.[51] The intensity ratio between D-band and G-band (I_D/I_G) is used to quantify the disorder degree of the sample.[52] In particular, I_D/I_G value of 0.82 is found for the CBSG sample. This number reveals a situation where the biochar shows both graphitic characteristics and disordered configuration, in agreement with the XRD analysis.

Generally speaking,[53] the degree of graphitization decreases with the increase in defects concentration (which is proportional to the ratio I_D/I_G). In this respect, N, O and S atoms cause a large number of defects in the carbon structures, in turn increasing the number of active sites dedicated to Li storage. Even though, when it comes to the overall electrochemical evaluation of a material, a trade-off needs to be identified between having a high number of defects and a high degree of ordered graphitic carbon, as both factors can contribute to the performance of the electrochemical cell. In particular, high disorder relates to higher initial capacities, whereas high graphitic order is associated to better cell stability, especially at high C-rates.[53,54] The N_2 adsorption–desorption (see Figure S2, Supporting Information) reveals a low specific surface area equal to 2.4 $m^2\ g^{-1}$ and a pore volume density of 0.036 $cm^3\ g^{-1}$ for the CBSG sample, hence exhibiting an isotherm curve which is typical of non-porous materials.[55] In good agreement with N_2 adsorption–desorption analysis, the FESEM image of Figure 1f shows a negligible porosity, thus suggesting that the pyrolysis process alone is not enough for designing porous structures. Although it is well known that high surface area can be beneficial for improving the capacity of carbon-based anodes,[41] recent studies have also reported about the use of non-porous carbonaceous materials as electrodes for LIBs.[44,56,57] Indeed, non-porous structures lead to a smaller consumption of electrolyte due to a thinner solid electrolyte interphase (SEI) layer formation and thus improving the initial coulombic efficiency and stability of biochar anodes.[44,56,58]

In order to investigate the structure and morphology of the lithium sulfide-graphene cathode, XRD analysis and electron microscopy (STEM and SEM) were carried out. **Figure 2**a shows the diffraction pattern of the $Li_2S70Gr30$ active material which reveals the presence of the characteristic peaks ascribed to the cubic Li_2S phase (ICDD: 98-006-0432, cyano bars). Moreover, it can also be identified the diffraction peaks typical of graphite (ICDD: 98-007-6767, red bars). The small residual peaks can be related to the presence of dilithium sulfate monohydrate (ICDD: 98-020-1530), probably due to the imperfect sealing of the kapton tape employed to prevent the contact with air. The SEM image

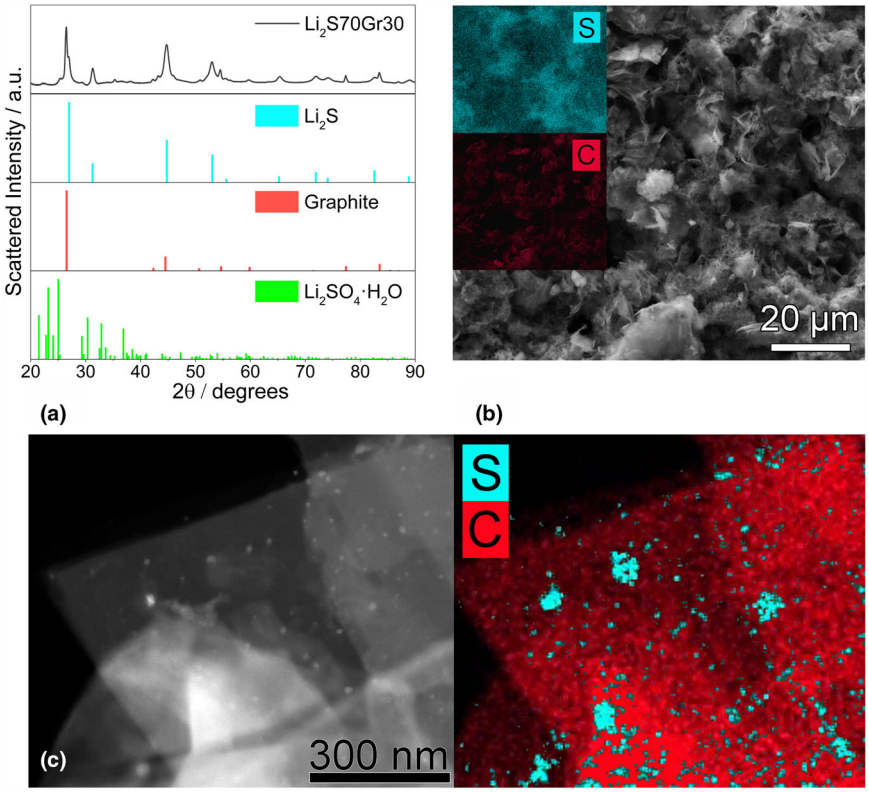

Figure 2. a) X-ray diffraction pattern of the Li2S70Gr30 active material and reference pattern of cubic lithium sulfide (ICDD: 98-006-0432, cyano bars), graphite (ICDD: 98-007-6767, red bars) and dilithium sulfate monohydrate (ICDD: 98-020-1530, green bars), b) SEM image of the $Li_2S70Gr30$ electrode and the relative EDS maps of sulfur and carbon, c) STEM image of the composite material (left side) and the related EDS map (red shades for carbon and cyan shades for sulfur).

of the composite electrode is reported in Figure 2b and the related elemental maps of sulfur and carbon are reported in the insets. The SEM image reveals the presence of graphene flakes with different dimensions covered by lithium sulfide particles which appear to be uniformly deposited on the carbonaceous surface. As suggested by the elemental EDS maps of sulfur (in inset, cyano shades), no evidence of sulfide aggregation is visible and the detected element presents a homogeneous overall distribution on the carbonaceous surface (in inset, red color).

Figure 2c shows the STEM image of the lithium sulfide-carbon composite and the corresponding EDS map. The STEM photo reveals the presence of small-sized lithium sulfides particles anchored on the graphene sheets surface, as confirmed by the EDS map. The Li_2S particles dimension is in the range 10–30 nm in diameter, and the particles are randomly distributed on the carbon-based substrate. The Li_2S particles diameter was also determined by employing the Scherrer equation, which confirmed the observed size range. The details of the calculation are reported in Supporting Information (see Eq. S1).

2.2. Electrochemical Characterization

2.2.1. Li/CBSG Half-Cell

The main goal of the present work is the design of a new kind of biochar-based anode to be employed in LiMF sulfur batteries. Thus, a preliminary analysis of the electrochemical performance of the CBSG electrode in lithium half-cell configuration was evaluated in an ether-based electrolyte. The negative electrodes present a loading of ~0.7–0.9 $mg_{(CBSG)}$ cm^{-2}. In particular, DOLDME-LITFSI-$LiNO_3$, the most common electrolyte in sulfur-based batteries, was employed also for this work. **Figure 3a** reports the CV behavior of the CBSG electrode. During the first cycle, the cathodic reduction curve reveals the presence of a peak at 1.7 V that can be correlated to the $LiNO_3$ decomposition.[59] The peak at around 0.55 V during the initial reduction is instead associated with SEI formation on the CBSG electrode surface due to the electrolyte degradation.[46,59] In the subsequent cycles, the aforementioned peaks (at 1.7 and 0.55 V) vanish, thus demonstrating the stability of the formed SEI film. Finally, the presence of two peaks at around 0 V (cathodic peak) and 0.2 V (anodic peak) correspond to the lithiation and the delithiation of CBSG electrode, respectively.[60] To be noted that the considerable overlap between the 3rd and 10th cycles discloses the low electrochemical polarization and the high reversibility of the designed electrode combined with the electrolyte of choice. To further electrochemically characterize the CBSG electrode in the ether-based electrolyte, rate capability and long-term cyclic stability at a specific current density were investigated. The rate capability test (Figure 3b,c) was carried out by increasing the current density from 0.1 to 2 A g^{-1} and then back down to 0.1 A g^{-1}, in order to check the capacity recovery after high current density analyses. The charge–discharge profiles of the CBSG electrode at increasing current densities are shown in Figure 3b while the specific discharge capacity versus cycle number is reported in Figure 3c. The Li/CBSG half-cell achieved a specific discharge capacity of 348, 271, 219, 212, 195, 152 mAh g^{-1} at 0.1, 0.2, 0.5, 0.7, 1, and 2 A g^{-1}, respectively, showing a coulombic efficiency approaching 99%. As expected, by increasing the current density the specific capacity is lowered probably due to a polarization growth, as can be noticed from Figure 3b. Once the current density is reset to 0.1 A g^{-1}, the CBSG electrode exhibits a stable capacity and a long cycling life (348 mAh g^{-1} over 315 cycling). In order to better comprehend which processes contribute to the stability of the Li/CBSG half-cell, EIS and ex situ SEM analyses were carried out and the results are reported in Figures S3 and S4, Supporting Information.

Figure S3, Supporting Information, depicts the Nyquist plot of the Li/CBSG half-cell at fresh state and after the rate capability test. The overall internal resistance of the cell decreases from 53.1 Ω in the fresh state down to 20 Ω after cycling, demonstrating an improvement in the cell kinetics. Indeed, this reduction could suggest a favorable movement of lithium ions within the CBSG electrode through the electrolyte and the SEI film.[61] The ex situ SEM analysis (top and cross-sectional views) of the CBSG is shown in Figure S4, Supporting Information, having the purpose of observing any structural change within the electrode due to the Li insertion and extraction after extensive cycling. The

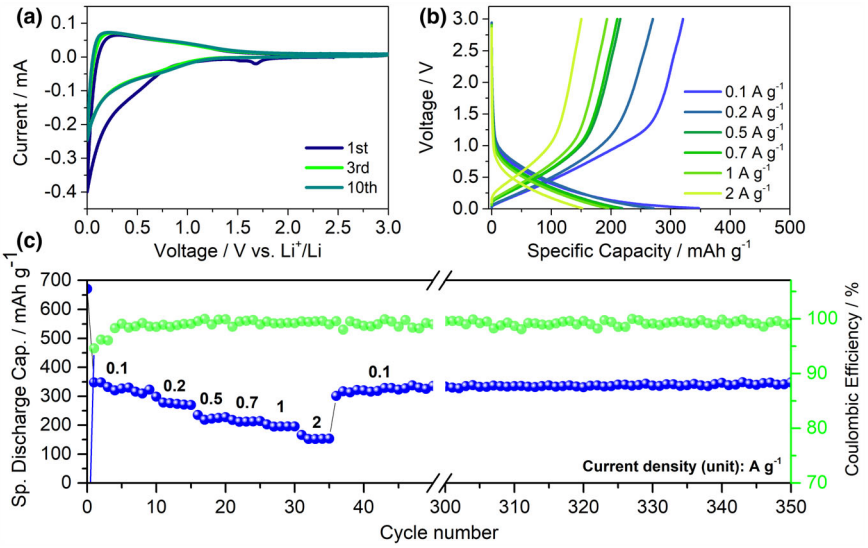

Figure 3. a) Cyclic voltammetry curves of CBSG at the scan rate of 0.1 mV s^{-1}, b) Galvanostatic charge–discharge profile relative to the 2nd cycle analyzed at each current density and c) Rate capability performance (discharge specific capacity upon cycling number and related coulombic efficiency) of CBSG at a current densities of 0.1, 0.2, 0.5, 0.7, 1, and 2 A g^{-1}. The tests were performed in the voltage range of 0.01–3 V at room temperature using a DOLDME-LITFSI-$LiNO_3$ as electrolyte.

morphological investigation suggests negligible volume changes and pulverization of the CBSG electrode after cycling, thus confirming the robustness and compatibility of the proposed anode material in the ether-based electrolyte. Moreover, the cycling performance of the Li/CBSG half-cell was also analyzed at 0.5 A g^{-1} (1.3 C-rate if compared with graphite), as shown in Figure S5, Supporting Information. The CBSG electrode shows a specific capacity around 205 mAh g^{-1} over 400 cycles, with a coulombic efficiency equal to ~99% and no visible capacity fading. Finally, Table S1, Supplementary Information, compares the performance achieved by our electrode versus graphite when conventional ether-based electrolyte is considered. The comparison highlights the superior electrochemical behavior of CBSG, especially capable of long cycling (>400 cycles) against few tens for graphite.

2.2.2. Li/Li_2S70Gr30 Half-Cell

Lithium-metal half-cells employing Li_2S70Gr30 as working electrode were tested in order to evaluate the electrochemical performance of the cathode active material. The loading of the positive electrodes is ~0.6 $mg_{(Li2S)}$ cm^{-2}. **Figure 4a** shows the CV measurements carried out on the Li_2S70Gr30 electrode in the 1.8–2.6 V voltage range at the scan rate of 0.1 mV s^{-1}. The CV profiles show the characteristic shape ascribed to the multistage reactions between lithium and elemental sulfur. It is noteworthy that no overpotential was necessary to overcome the initial activation barrier, probably due to the small Li_2S particles size and the presence of highly conductive carbonaceous material within the composite.

The first anodic peak at about 2.35 V in the first cycle appears in the following cycles at the same voltage while the second anodic peak initially at 2.5 V shifts to a lower value (2.4 V vs Li^+/Li) in the following cycles. This latter effect could be ascribed to overpotential reduction subsequent to the initial Li_2S activation. The overall anodic curve could be ascribed to the oxidation of Li_2S to elemental sulfur (S_8). These reactions involve the conversion of Li_2S into low-order polysulfide moieties Li_2S_x ($2< \times \leq 6$) and successively to long-chain species Li_2S_x ($6< \times \leq 8$). In the cathodic scan two reduction peaks appear at 2.4 V and at about 2.0 V, indicating the reversibility of the reaction from S_8 to Li_2S through the formation of PSs species. Figure 4b,c report the galvanostatic cycling test carried out at 1C (1166 mA g^{-1}) showing the specific capacity versus cycle number and the relative voltage profiles, respectively.

Figure 4b reveals an initial capacity of 805 mAh g^{-1} (with respect to Li_2S mass). This value was achieved by cycling the cell at C/10 for the first cycle in order to activate the oxidation reaction and thus avoiding the application of a high voltage cut-off (overpotential) to overcome the energy barrier for the Li_2S oxidation. At 1C, the cell specific capacity reaches a value of 580 mAh g^{-1}, then slowly decreases during cycling to reach a capacity of 340 mAh g^{-1} after 350 cycles.

Figure 4c shows the voltage profile relative to the 1C galvanostatic cycling test. In particular, the curve referring to the first cycle at C/10 shows a small charge overpotential, as indicated by the red circle and highlighted in the inset. The following cycles at 1C depict the characteristic voltage profiles of the lithium-sulfur chemistry reactions. Indeed, the charge curves show a plateau at about 2.35 V which is ascribed to the oxidation of Li_2S to elemental sulfur. Two main redox plateaus are present upon discharge at about 2.35 V and 2.0 V, representing the conversion of S_8 into its discharge product (i.e., Li_2S_2 and Li_2S). It is also observed a slow increase in the voltage hysteresis along the whole test suggesting a small capacity drop upon cycling.

2.2.3. CBSG/Li_2S70Gr30 Full-Cell

In order to explore the eligibility of the biochar electrode as metallic-lithium substitute in a full-cell configuration, the CBSG electrode was employed as negative electrode in a LiMF sulfur battery. Before the full-cell assembly, the CBSG electrode was prelithiated following the procedure mentioned in the Experimental Section (see also Scheme S1, Supporting Information). The prelithiation process leads to the SEI formation on the electrode surface thus improving the initial coulombic efficiency, reversibility, and cyclic stability of the whole cell.[62] **Figure 5a,b** report the rate capability performance of the CBSG/Li_2S70Gr30 cell showing the specific discharge capacity versus cycle number and the voltage profiles, respectively. The test was carried out by increasing the current from 0.05C to 1C (=1166 mA g^{-1}) through 0.1 and 0.5C over 400 cycles. During the first charging cycle, a small initial activation potential at ~2.4 V is required in order to completely extract the Li ions from Li_2S, resulting in a hump shown in the first charge profile of Figure 5b. The same behavior was observed in Figure 4c and it is related to the activation of Li_2S. In order to confirm this phenomenon, the differential capacity-voltage profile and CV test (See Figure S6, Supporting Information) were analyzed. Here, the presence

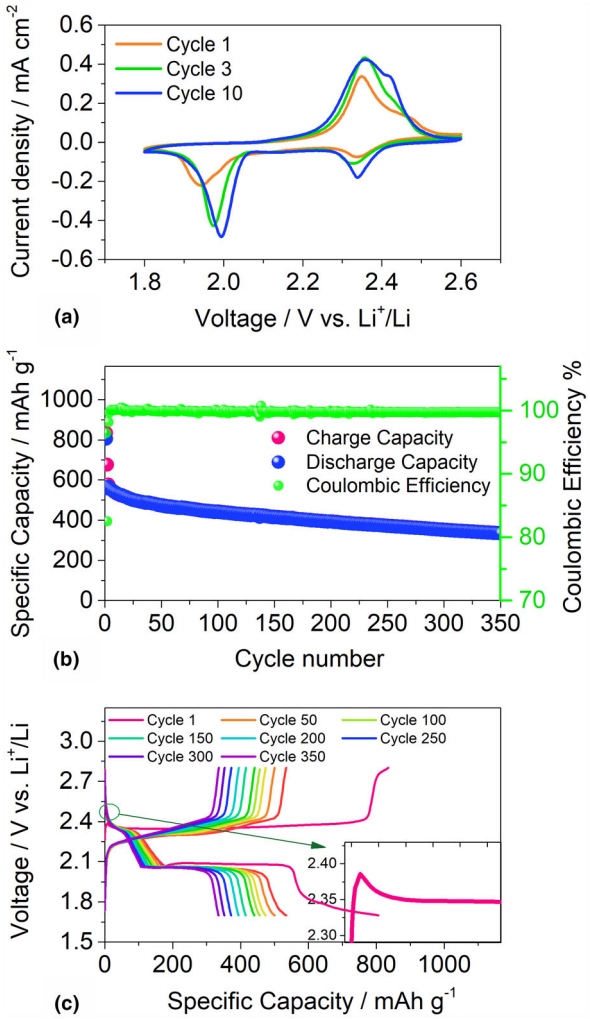

Figure 4. a) Cyclic voltammetry tests of $Li_2S70Gr30$ electrode, performed in 2032-coin cell using DOLDME-LITFSI-$LiNO_3$ as electrolyte in 1.8 V – 2.6 V voltage range with a scan rate of 0.1 mV s^{-1}. b) Galvanostatic cycling profiles and c) voltage profiles of the $Li_2S70Gr30$ electrode performed in 2032-coin cells with DOLDME-LITFSI-$LiNO_3$ electrolyte carried out at 1C = 1166 mA g^{-1} after running the first cycle at C/10 within the voltage limits of 1.7–2.8 V.

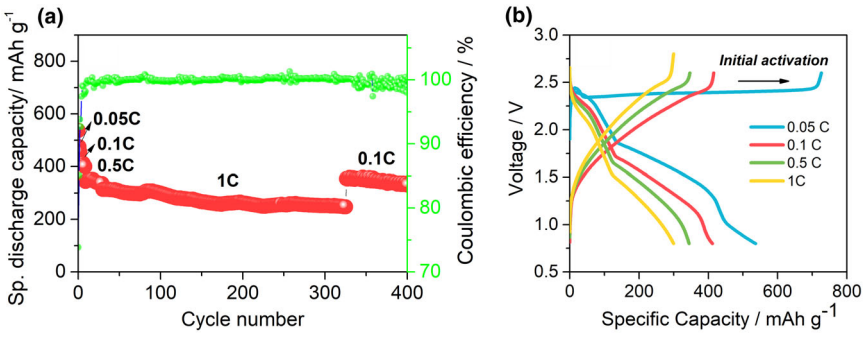

Figure 5. a) Long rate cycling (discharge specific capacity upon cycle number and related coulombic efficiency) of CBSG/$Li_2S70Gr30$ full-cell. The specific capacity of the cell is reported considering the Li_2S mass. All the tests are performed in the voltage range of 0.8–2.6 V at room temperature. Electrolyte: DOLDME-LITFSI-$LiNO_3$. b) Corresponding charge–discharge profiles.

of a sharp peak appearing during the $Li_2S70Gr30$ oxidation, corroborates the hypothesis of the activation of the nano-sized Li_2S at 2.4 V. The charge–discharge profiles of Figure 5b reveal an initial charge and discharge capacity of 726 and 537 mAh g^{-1} at 0.05C, respectively, resulting in an initial coulombic efficiency of 74%. The cell energy density at the first cycle reaches 872 Wh Kg^{-1} based on the cathode mass, whereas when considering both the electrodes it is ~370 Wh Kg^{-1}. Furthermore, by increasing the current rate, and consequently the cell polarization,[9] the CBSG/$Li_2S70Gr30$ shows a capacity of 412, 350, and 300 mAh g^{-1} at 0.1, 0.5 and 1C, respectively. Interestingly, the cell delivered 73% of 0.1C capacity at 1C demonstrating a stable profile for 300 consecutive cycles with a coulombic efficiency approaching 100%, as shown in Figure 5a. Moreover, it is worth noticing that, once the current is set back to 0.1C, the cell recovered a discharge capacity of ~355 mAh g^{-1} thus indicating the superior reversibility and cycling stability of the CBSG/$Li_2S70Gr30$ system.

A galvanostatic charge–discharge test at 1C was carried out on the CBSG/$Li_2S70Gr30$ full-cell and the results are reported in Figure S7, Supporting Information. The full-cell reveals a relatively stable behavior upon cycling, with an initial discharge capacity of 280 mAh g^{-1} which slowly decreases down to 210 mAh g^{-1} after 350 cycles. The formation of a stable SEI layer on the CBSG surface could be responsible for the reduction of the PS shuttle effect thus leading to the observed performance.[63]

Finally, in **Table 2** the main electrochemical results of the CBSG/$Li_2S70Gr30$ full-cell are compared with the data obtained for LiMF batteries exploiting Li_2S as cathodic active material. Based on the data reported in Table 2, we can draw the conclusion that the strategy proposed in this study offers a novel and promising method to design sustainable and cost-effective electrodes for the next-generation of LIBs.

3. Conclusion

A new pathway is herein proposed to achieve high efficient, environment friendly and safe lithium-metal free (LiMF) sulfur batteries, with the main purpose of avoiding the negative impact of metallic lithium for application in LSBs. In this study, an eco-friendly and low-cost material based on brewer's spent grain (BSG) is employed as anodic active material for application in sulfur full-cell configuration. The inherently N- and O-doped biochar showed a stable electrochemical behavior in conventional ether-based electrolyte. The wide average interlayer spacing, the presence of pyridinic/quaternary N atoms along with oxygen-containing groups, and the cross-linked carbonaceous clusters within the biochar material translated into superior electrochemical performance. Moreover, a Li_2S-few layer graphene-based composite material was designed through a simple recrystallization method for the synthesis of the positive electrode. This composite material was activated through an initial low C-rate cycle, without requiring the application of a high potential. LiMF cells were then assembled by coupling the prelithiated CBSG and the $Li_2S70Gr30$ composite, used as anode and cathode, respectively. The designed LiMF cell showed an initial charge and discharge capacities of 726 and 537 mAh g^{-1} with a

Table 2. Electrochemical performance of LiMF sulfur batteries (full-cell) based on lithium sulfide cathode.

Cathode	Anode	Average working voltage (V)	Capacity (mAh g^{-1}) @ cycle number	References
Li_2S70Gr30	CBSG	~1.7 at 0.1C	~340 @ 400 at 0.1C (after cycling at various C-rates), and ~210 @ 350 at 1C	This work
Li_2S@MCMB	Si-O-C material	~1.4 at 0.2C	~280 @ 50 at 0.2C	[64]
Thermally exfoliated graphene–Li_2S	Si thin film	~1.6 at 1C	~450 @ 30 at 1C	[25]
Li_2S@C composite	Graphite–solid electrolyte composite	~2 at 0.01C	~650 @ 10 at 0.01C	[65]
Li_2S@porous carbon	Graphite	~1.9 at 0.1C	~268 @ 30 at 0.1C ~173 @ 100 at 0.5C	[66]
Li_2S@graphene nanocapsule	Graphite	~1.8 at 0.1C	~440 @ 200 at 0.1C	[19]
Li_2S@MXene/graphene	Fe_3O_4/CNs	~1.7 at 0.2C	~430 @ 50 at 0.2C	[30]
Li_2S-rGO	MnO_2-rGO	~1.7 at 0.2C	~470 @ 150 at 0.2C	[29]
Li_2S@Carbon aerogel	TiO_2	~2.3 at 0.1C	370 @ 200 at 0.1C	[67]
Li_2S@Carbon aerogel	Graphene	~2.2 at 0.1C	200 @ 200 at 0.1C	[67]
Li_2S	Si-C	-	Very low @ 200 at 1C	[68]
Mo-Li_2S-graphene	Si-C	~2.2	463 @ 200 at 1C	[68]

coulombic efficiency of 74%. The reported system demonstrated excellent cycling stability upon Li insertion/de-insertion during the electrochemical tests. This work offers the first-reported approach for designing sulfur batteries based on a biochar anode. However, further optimization is still needed to develop fast-charging LiMF based on sulfur chemistry, a crucial aspect for the EVs performance improvement.

4. Experimental Section

Materials synthesis: Synthesis of CBSG—Carbonized brewer's spent grain was obtained by employing a laboratory-scale prototype plant (Carbolite custom model EVT 12/450B), as reported in a previous article of ours.[53] The pyrolysis of BSG (<2 mm in size) was carried out by heating up the sample till 700 °C at 5 °C/min under a 100 mL/min nitrogen flow. The temperature was maintained constant at 700 °C for 30 min. Afterward, the CBSG powder was centrifuged in a 1.0 M HCl solution, then grinded and sieved down to ~90 µm.

Synthesis of Li_2S70Gr30—Lithium sulfide-graphene active material was prepared in an inert atmosphere by an easy solvent evaporation method. In an argon-filled glove box (MBraun), lithium sulfide from Sigma Aldrich and graphene, the latter prepared via liquid-phase exfoliation of graphite from NEI, were mixed in a 70:30 weight ratio in a flask using anhydrous ethanol as solvent, which was dried under molecular sieves for several days. Successively, the solution was sonicated for 1.5 h in a sonic bath. The solvent was then removed by heating it up to 60 °C under vacuum pressure of 400 mbar. All the process was carried out without exposing the sample to the air. The as-obtained powder was collected and stored in a glove box for cathode preparation.

Materials characterization: The chemical structure and the heteroatoms binding states of the CBSG sample were analyzed by X-ray photoelectron spectroscopy (XPS) using Kratos Axis Ultra DLD spectrometer equipped with a monochromatic Al Kα source (15 kV, 20 mA). The total carbon, nitrogen, hydrogen, and sulfur (CHNS) contents of the CBSG active material were measured by UNICUBE organic elemental analyzer (from Elemental) and the oxygen content was calculated by the difference. The ash content was determined following the ASTM-D1102 protocol. The surface functionality of CBSG was investigated by Fourier Transform Infrared Spectroscopy (FTIR) using Perkin Elmer Spectrum One spectrometer with a wavenumber range of 400–4000 cm^{-1} at room temperature with a resolution of 4 cm^{-1}. Pellets were prepared by thoroughly mixing the carbon sample and KBr. In order to determine the crystallinity, presence of minerals, and order/disorder degree of the samples structure, a Malvern PANalytical Empyrean X-ray diffractometer (XRD) equipped with a 1.8 kW CuKα sealed ceramic tube and a Renishaw in Via Micro Raman equipped with a laser source of 532 nm were used. Moisture-sensitive sample (Li_2S powder) was covered with Kapton tape in order to reduce the exposure to air. The surface morphology of the CBSG powder and electrodes were analyzed by means of field-emission scanning electron microscopy (FESEM) (JEOL JSM-7500FA). Li_2S70Gr30 active material powder was investigated by scanning electron microscopy (SEM) and energy dispersive spectroscopy (EDS) using a JEOL JSM-6490LA SEM Analytical (low-vacuum) operating at an acceleration voltage of 5 kV with a W filament thermionic source. Scanning transmission electron microscopy (STEM) images and energy dispersion spectroscopy (EDS) maps were acquired with a JEM 1400 Plus (JEOL) provided with a thermionic source (LaB_6) and applying an acceleration voltage of 120 kV.

Electrode and electrolyte preparation: CBSG electrode preparation—The CBSG electrodes were prepared by mixing 70 wt% of the active material (CBSG), 15 wt% of conductive carbon black agent (Imerys), and 15 wt% of carboxymethylcellulose (CMC, Dalian Chem) working as binder. After grinding evenly, the mixture was mechanically stirred in deionized water to form a slurry. Successively, the film electrode was casted on a copper foil (10 µm thickness) by using Doctor-Blade technique and dried on a hot plate for 3 h at 60 °C. After drying, the electrodes were punched into 15 mm diameter disks and further dried using a Buchi apparatus for 4 h at 80 °C. Subsequently, the prepared electrodes

were stored in an argon-filled glove box (MBraun). The active mass loading was about 0.7–0.9 $mg_{(CBSG)}$ cm^{-2}.

$Li_2S70Gr30$ electrode preparation—The positive electrodes were prepared in an argon-filled glove box by mixing the lithium sulfide-graphene active material ($Li_2S70Gr30$) with Super P carbon (from Imerys) as a conductive agent, polyvinylidene difluoride PVdF (from Solvay) as binder in 80:10:10 weight ratio in a mortar. N-methylpyrrolidone (NMP, from Sigma Aldrich) was used as solvent for slurry preparation. The slurry was casted by Doctor-Blade onto a carbon cloth current collector (AvCarb) and dried overnight at 40 °C. The electrode foils were punched into 14 mm diameter disks. The lithium sulfide content within the active material is 70%, while the mass loading of the final electrode (considering the 80% of active material in total) is ~0.6 $mg_{(Li2S)}$ cm^{-2}.

Electrolyte preparation—A solution containing 1 mol kg^{-1} (m) of lithium bis (trifluoromethanesulfonyl)imide (LiTFSI, Sigma–Aldrich) and 0.5 mol kg^{-1} (m) of lithium nitrate ($LiNO_3$, Sigma–Aldrich) dissolved in 1,3-dioxolane (DOL, Sigma–Aldrich) and 1,2-dimethoxyethane (DME, Sigma–Aldrich) solvents (weight ratio, 1:1) was used as electrolyte for electrochemical characterization (from here on named DOLDME-LITFSI-$LiNO_3$). Before the electrolyte preparation, the DOL and DME solvents were dried over molecular sieves for 10 days. The prepared electrolytic solution was stirred in an MBraun argon-filled glovebox for 24 h.

Electrochemical characterization: The electrochemical characterization was performed by employing 2032 coin cells. The amount of electrolyte was ≈15 $\mu L_{electrolyte}/mg_{active\ material}$ for both half-cell and full-cell measurements. A microporous polymeric membrane (Celgard 2400) was used as a separator for the electrochemical tests. In addition, for the electrochemical analyses of Li/CBSG and Li/$Li_2S70Gr30$ half-cells, lithium chips (15.6 mm, MTI Corporation) were used as reference and counter electrode. The cells were assembled in an argon-filled MBraun glovebox with H_2O and O_2 levels lower than 0.1 ppm. The Li/CBSG half-cells were analyzed with constant current (CC) protocol in the voltage range of 0.01–3 V at the current densities of 0.1, 0.2, 0.5, 0.7, 1, and 2 A g^{-1}. The current density was calculated based on the active material weight of the CBSG electrode. Li/$Li_2S70Gr30$ half-cells were galvanostatically characterized at 1C (1166 mA g^{-1}) in the 1.7–2.8 V range. An activation cycle at 0.1C was carried out in order to promote the Li_2S conversion into S_8. The cyclic voltammetry (CV) measurement of the lithium-metal half-cells was carried out at the scan rate of 0.1 mV s^{-1} in the 0.01–3 V and 1.8–2.6 V voltage ranges for CBSG and $Li_2S70Gr30$ electrodes, respectively. Electrochemical Impedance Spectroscopy (EIS) technique was used for Li/CBSG half-cells in the frequency range from 10 kHz to 100 mHz with a 10 mV alternating current. In order to assemble the full-cells, a direct contact electrochemical method (DC-EM)[69] was used to prelithiate the CBSG electrode by keeping it in direct contact with a metallic Li chip in presence of the electrolyte for 8 h (see Scheme S1, Supporting Information). Subsequently, the lithiated CBSG electrode was rinsed with DME solvent and dried in an inert environment. Afterward, the lithiated CBSG/$Li_2S70Gr30$ full-cell was assembled according to the mass ratio of 1:1.35, corresponding to the active material weights of $Li_2S70Gr30$:CBSG. The initial capacity of each electrode at low current density/rate in half-cell configuration was considered for the mass balancing. The galvanostatic cycling test of CBSG/$Li_2S70Gr30$ full-cell was carried out at the current rates of 0.05C (58 mA g^{-1}), 0.1C (116 mA g^{-1}), 0.5C (583 mA g^{-1}), and 1C (1166 mA g^{-1}) in the voltage range 0.8–2.6 V. The specific gravimetric capacities of Li/$Li_2S70Gr30$ half-cells and CBSG/$Li_2S70Gr30$ full-cells were calculated based on the Li_2S mass. The CV analysis of the CBSG/$Li_2S70Gr30$ full cell was performed between 0.8 and 3 V at the scan speed of 0.1 mV s^{-1}. The whole electrochemical characterization was obtained at room temperature by employing a BCS-805 multichannel battery unit by BioLogic.

Acknowledgement

P.S. and E.V. contributed equally to this work. The authors thank to Simone Lauciello and Luca Leoncino from the IIT Electron Microscopy Facility for FESEM characterization and STEM analyses. R.P.Z. wishes to recognize support from the Natural Science Foundation of China, grant no. 32071317.

Conflict of Interest

The authors declare no conflict of interest.

Supporting Information

Supporting Information is available from the Wiley Online Library or from the author.

Keywords

biochars, ether-based electrolytes, lithium sulfide, lithium-metal free batteries, superior cycling stability

Received: August 24, 2022
Revised: November 26, 2022
Published online: November 29, 2022

[1] Z. P. Cano, D. Banham, S. Ye, A. Hintennach, J. Lu, M. Fowler, Z. Chen, *Nat. Energy* **2018**, *3*, 279.
[2] L. Canals Casals, E. Martinez-Laserna, B. Amante García, N. Nieto, *J. Clean. Prod.* **2016**, *127*, 425.
[3] A. Moro, L. Lonza, *Transp. Res. Part D Transp. Environ.* **2018**, *64*, 5.
[4] S. Javadian, Z. Parviz, P. Salimi, M. Nasrollahpour, H. Gharibi, H. Kashani, A. Morsali, R. P. Zaccaria, *J. Alloys Compd.* **2022**, *898*, 162849.
[5] S. Javadian, P. Salimi, H. Gharibi, A. Fathollahi, E. Kowsari, J. Kakemam, *J. Iran. Chem. Soc.* **2019**, *16*, 2123.
[6] W. Li, R. Long, H. Chen, J. Geng, *Renew. Sust. Energ. Rev.* **2017**, *78*, 318.
[7] D. Tian, X. Song, Y. Qiu, X. Sun, B. Jiang, C. Zhao, Y. Zhang, X. Xu, L. Fan, N. Zhang, *Energy Environ. Mater.* **2021**, DOI: 10.1002/eem2.12236.
[8] J. Hassoun, B. Scrosati, *Angew. Chemie* **2010**, *122*, 2421.
[9] Z. H. Chen, X. L. Du, J. B. He, F. Li, Y. Wang, Y. L. Li, B. Li, S. Xin, *ACS Appl. Mater. Interfaces* **2017**, *9*, 33855.
[10] W. J. Chen, C. X. Zhao, B. Q. Li, Q. Jin, X. Q. Zhang, T. Q. Yuan, X. Zhang, Z. Jin, S. Kaskel, Q. Zhang, *Energy Environ. Mater.* **2020**, *3*, 160.
[11] F. Xu, X. Li, F. Xiao, S. Xu, X. Zhang, P. He, H. Zhou, *Mater. Technol.* **2016**, *31*, 517.
[12] J. Jiang, Q. Fan, S. Chou, Z. Guo, K. Konstantinov, H. Liu, J. Wang, *Small* **2019**, DOI: 10.1002/smll.201903934.
[13] L. Carbone, J. Peng, M. Agostini, M. Gobet, M. Devany, B. Scrosati, S. Greenbaum, J. Hassoun, *ChemElectroChem* **2017**, *4*, 209.
[14] E. Venezia, P. Salimi, S. Chauque, R. Proietti Zaccaria, *Nanomaterials* **2022**, *12*, 3933.
[15] D. Su, D. Zhou, C. Wang, G. Wang, *Adv. Funct. Mater.* **2018**, DOI: 10.1002/adfm.201800154.
[16] A. Manthiram, Y. Fu, S. Chung, C. Zu, Y. Su, **2014**, *114*, 11751.
[17] H. Jha, I. Buchberger, X. Cui, S. Meini, H. A. Gasteiger, *J. Electrochem. Soc.* **2015**, *162*, A1829.
[18] Z. Li, Y. Kamei, M. Haruta, T. Takenaka, A. Tomita, T. Doi, S. Zhang, K. Dokko, M. Inaba, M. Watanabe, *Electrochemistry* **2016**, *84*, 887.
[19] G. Tan, R. Xu, Z. Xing, Y. Yuan, J. Lu, J. Wen, C. Liu, L. Ma, C. Zhan, Q. Liu, T. Wu, Z. Jian, R. Shahbazian-Yassar, Y. Ren, D. J. Miller, L. A. Curtiss, X. Ji, K. Amine, *Nat. Energy* **2017**, DOI: 10.1038/nenergy.2017.90.
[20] G. Zhou, E. Paek, G. S. Hwang, A. Manthiram, *Adv. Energy Mater.* **2016**, DOI: https://utw10370.utweb.utexas.edu/publications/P163.pdf.
[21] H. El-Shinawi, E. J. Cussen, S. A. Corr, *Nanoscale* **2019**, *11*, 19297.
[22] A. Hayashi, R. Ohtsubo, M. Tatsumisago, *Solid State Ion.* **2008**, *179*, 1702.
[23] L. Zhou, W. Zhang, Y. Wang, S. Liang, Y. Gan, H. Huang, J. Zhang, Y. Xia, C. Liang, *J. Chem.* **2020**, *2020*, 6904517.
[24] M. R. Kaiser, Z. Han, J. Liang, S. X. Dou, J. Wang, *Energy Storage Mater.* **2019**, DOI: 10.1016/j.ensm.2019.04.001.
[25] K. Zhang, L. Wang, Z. Hu, F. Cheng, J. Chen, *Sci. Rep.* **2014**, DOI: 10.1038/srep06467.

[26] Y. Li, S. Guo, *Matter* **2021**, *4*, 1142.
[27] Y. Yang, G. Zheng, S. Misra, J. Nelson, M. F. Toney, Y. Cui, *J. Am. Chem. Soc.* **2012**, *134*, 15387.
[28] F. Ye, H. Noh, H. Lee, H. T. Kim, *Adv. Sci.* **2018**, DOI: 10.1002/advs.201800139.
[29] Y. Chen, S. Lu, Y. Li, W. Qin, X. Wu, *Mater. Lett.* **2019**, *248*, 157.
[30] Z. Wang, N. Zhang, M. Yu, J. Liu, S. Wang, J. Qiu, *J. Energy Chem.* **2019**, *37*, 183.
[31] J. Hassoun, B. Scrosati, *Angew. Chem. Int. Ed.* **2010**, *49*, 2371.
[32] S. Wang, H. Chen, Z. Zhong, X. Hou, S. Hu, J. Wu, *Ionics (Kiel).* **2018**, *24*, 3385.
[33] S. S. J. Aravind, V. Eswaraiah, S. Ramaprabhu, *J. Mater. Chem.* **2011**, *21*, 17094.
[34] E. V. Soares, H. M. V. M. Soares, *Appl. Microbiol. Biotechnol.* **2021**, *105*, 1379.
[35] A. Manuja, B. Kumar, R. Kumar, D. Chhabra, M. Ghosh, M. Manuja, B. Brar, Y. Pal, B. N. Tripathi, M. Prasad, *Toxicol. Rep.* **1970**, *2021*, 8.
[36] P. Zeng, Y. Han, X. Duan, G. Jia, L. Huang, Y. Chen, *Mater. Res. Bull.* **2017**, *95*, 61.
[37] D. Lv, P. Yan, Y. Shao, Q. Li, S. Ferrara, H. Pan, G. L. Graff, B. Polzin, C. Wang, J. G. Zhang, J. Liu, J. Xiao, *Chem. Commun.* **2015**, *51*, 13454.
[38] X. Li, J. Liang, W. Li, J. Luo, X. Le, X. Yang, Y. Hu, Q. Xiao, W. Zhang, R. Li, T. K. Sham, X. Sun, *Chem. Mater.* **2019**, *31*, 2002.
[39] R. Deng, M. Wang, H. Yu, S. Luo, J. Li, F. Chu, B. Liu, F. Wu, *Energy Environ. Mater.* **2022**, *5*, 777.
[40] F. Yu, S. Li, W. Chen, T. Wu, C. Peng, *Energy Environ. Mater.* **2019**, *2*, 55.
[41] O. Norouzi, P. Salimi, F. Di Maria, S. Pourhosseini, F. Safari, in *Production of Materials from Sustainable Biomass Resources* (Eds: Z. Fang, R. Smith, Jr, Tian, X. F., Springer, Singapore **2019**, pp. 233–265.
[42] P. Salimi, O. Norouzi, S. E. M. Pourhosseini, *J. Alloys Compd.* **2019**, *786*, 930.
[43] S. E. M. Pourhosseini, O. Norouzi, P. Salimi, H. R. Naderi, *ACS Sustain. Chem. Eng.* **2018**, *6*, 4746.
[44] F. Luna-Lama, D. Rodríguez-Padrón, A. R. Puente-Santiago, M. J. Muñoz-Batista, A. Caballero, A. M. Balu, A. A. Romero, R. Luque, *J. Clean. Prod.* **2019**, *207*, 411.
[45] S. Huang, Z. Li, B. Wang, J. Zhang, Z. Peng, R. Qi, J. Wang, Y. Zhao, *Adv. Funct. Mater.* **2018**, DOI: 10.1002/adfm.201706294.
[46] H. Shan, X. Li, Y. Cui, D. Xiong, B. Yan, D. Li, A. Lushington, X. Sun, *Electrochim. Acta* **2016**, *205*, 188.
[47] W. Yu, H. Wang, S. Liu, N. Mao, X. Liu, J. Shi, W. Liu, S. Chen, X. Wang, *J. Mater. Chem. A* **2016**, *4*, 5973.
[48] J. Brückner, S. Thieme, F. Böttger-Hiller, I. Bauer, H. T. Grossmann, P. Strubel, H. Althues, S. Spange, S. Kaskel, *Adv. Funct. Mater.* **2014**, *24*, 1284.
[49] M. Lu, W. Yu, J. Shi, W. Liu, S. Chen, X. Wang, H. Wang, *Electrochim. Acta* **2017**, *251*, 396.
[50] J. R. Dahn, T. Zheng, Y. Liu, J. S. Xue, *Science (80-.)* **1995**, *270*, 590.
[51] X. Lian, Z. Sun, Q. Mei, Y. Yi, J. Zhou, M. H. Rümmeli, J. Sun, *Energy Environ. Mater.* **2022**, *5*, 344.
[52] P. Salimi, S. Javadian, O. Norouzi, H. Gharibi, *Environ. Sci. Pollut. Res.* **2017**, *24*, 27974.
[53] P. Salimi, S. Tieuli, S. Taghavi, E. Venezia, S. Fugattini, S. Lauciello, M. Prato, S. Marras, T. Li, M. Signoretto, P. Costamagna, R. Proietti Zaccaria, *Green Chem.* **2022**, *24*, 4119.
[54] J. Tu, L. Hu, S. Jiao, J. Hou, H. Zhu, *Phys. Chem. Chem. Phys.* **2013**, *15*, 18549.
[55] S. Wacharasindhu, S. Likitmaskul, L. Punnakanta, K. Chaichanwatanakul, K. Angsusingha, C. Tuchinda, *J. Med. Assoc. Thai.* **1998**, *81*, 420.
[56] M. Gao, K. Zou, Y. Deng, Z. Zhao, Y. Li, G. Chen, *ACS Appl. Mater. Interfaces* **2017**, *9*, 28527.
[57] W. Luo, C. Bommier, Z. Jian, X. Li, R. Carter, S. Vail, Y. Lu, J. J. Lee, X. Ji, *ACS Appl. Mater. Interfaces* **2015**, *7*, 2626.
[58] Y. Li, S. Xu, X. Wu, J. Yu, Y. Wang, Y. S. Hu, H. Li, L. Chen, X. Huang, *J. Mater. Chem. A* **2015**, *3*, 71.
[59] L. Carbone, M. Gobet, J. Peng, M. Devany, B. Scrosati, S. Greenbaum, J. Hassoun, *J. Power Sources* **2015**, *299*, 460.
[60] X. Zhang, C. Fan, P. Xiao, S. Han, *Electrochim. Acta* **2016**, *222*, 221.
[61] P. Salimi, E. Kowsari, *J. Electron. Mater.* **2019**, *48*, 2254.
[62] D. I. Lee, H.-W. Yang, W. S. Kang, J. Kim, S.-J. Kim, *J. Electrochem. Soc.* **2019**, *166*, A787.
[63] S. Thieme, J. Brückner, A. Meier, I. Bauer, K. Gruber, J. Kaspar, A. Helmer, H. Althues, M. Schmuck, S. Kaskel, *J. Mater. Chem. A* **2015**, *3*, 3808.
[64] M. Agostini, J. Hassoun, J. Liu, M. Jeong, H. Nara, T. Momma, T. Osaka, Y. K. Sun, B. Scrosati, *ACS Appl. Mater. Interfaces* **2014**, *6*, 10924.
[65] T. Takeuchi, H. Kageyama, K. Nakanishi, T. Ohta, A. Sakuda, T. Sakai, H. Kobayashi, H. Sakaebe, K. Tatsumi, Z. Ogumi, *Solid State Ion.* **2014**, *262*, 138.
[66] N. Wang, N. Zhao, C. Shi, E. Liu, C. He, F. He, L. Ma, *Electrochim. Acta* **2017**, *256*, 348.
[67] R. K. Bhardwaj, H. Lahan, V. Sekkar, B. John, A. J. Bhattacharyya, *ACS Sustain. Chem. Eng.* **2022**, *10*, 410.
[68] J. Zhang, J. Wang, M. Qian, B. Zhao, R. Wang, X. Hao, X. Huang, R. Shao, Z. Xing, J. Xie, B. Xu, Y. Su, F. Wu, G. Tan, *Adv. Funct. Mater.* **2022**, *32*, 1.
[69] L. Jin, C. Shen, Q. Wu, A. Shellikeri, J. Zheng, C. Zhang, J. P. Zheng, *Adv. Sci.* **2021**, DOI: 10.1002/advs.202005031.